Metal-Carbodithioate based 3D Semiconducting Metal-Organic Framework: Porous Optoelectronic Material for Energy Conversion

Xinlin Li,[a] Ryther Anderson,[b] H. Christopher Fry,[c] Saied Md Pratik,[d] Wenqian Xu,[e] Subhadip Goswami,[f] Taylor G. Allen,[g] Jierui Yu,[a] Sreehari Surendran Rajasree,[a] Christopher J. Cramer,[d] Garry Rumbles,[g,h] Diego A. Gómez-Gualdrón,*,[b] and Pravas Deria*,[a]

[a] School of Chemical and Biomolecular Science, Southern Illinois University, 1245 Lincoln Drive, Carbondale, Illinois 62901, United States.

[b] Department of Chemical and Biological Engineering, Colorado School of Mines, 1601 Illinois St, Golden, Colorado 80401, United States.

[c] Center for Nanoscale Materials, Argonne National Laboratory, 9700 S Cass Ave, Lemont, Illinois 60439, United States.

[d] Department of Chemistry, Minnesota Supercomputing Institute, and Chemical Theory Center, University of Minnesota, 207 Pleasant St SE, Minneapolis, Minnesota 55455, United States.

[e] X-ray Science Division, Advanced Photon Source, Argonne National Laboratory, 9700 S Cass Ave, Lemont, Illinois 60439, United States.

[f] Department of Chemistry, Northwestern University, 2145 Sheridan Road, Evanston, Illinois 60208, United States.

[g] National Renewable Energy Laboratory, 15013 Denver West Parkway, Golden, Colorado 80401, United States

[h] Renewable and Sustainable Energy Institute, Department of Chemistry, University of Colorado, Boulder, Colorado 80309, United States

KEYWORDS: through-bond conductivity, metal-carbodithioate linkage, metal-organic framework, light-harvesting, photoelectrocatalysis

ABSTRACT: Solar-energy-conversion requires the working compositions to generate photoinduced charges with high potential and the ability to deliver charges to the catalytic sites and/or external electrode. These two properties are typically at odds with each other and call for new molecular materials with sufficient conjugation to improve charge conductivity, but not as much conjugation as to overly compromise the optical bandgap. In this work, we developed a semiconducting MOF prepared explicitly through metal-carbodithioate '$(\text{—}CS_2)_nM$' linkage chemistry, entailing augmented metal-linker electronic communication. The stronger ligand field and higher covalent character of metal-carbodithioate linkages—when combined with spirofluorene-derived organic struts and nickel (II) ions-based node—provided a stable, semiconducting 3D-porous MOF, Spiro-CS_2Ni. This MOF lacks long-range ordering and is defined by a flexible structure with non-aggregated building units, as suggested by reverse-Monte Carlo simulations of the pair distribution function obtained from total scattering experiments. The solvent-removed 'closed pore' material recorded a BET area of ~400 m^2/g, where the 'open pore' form possesses a 90 wt% solvent-accessible porosity. Electrochemical measurements suggest that Spiro-CS_2Ni possess a bandgap of 1.57 eV (σ =10^{-7} S/cm at -1.3V bias potential), which can be further improved by manipulating the *d*-electron configuration through an axial-coordination (ligand/substrate), the latter which indicates usefulness as an electro and/or photoelectrocatalyst (through substrate binding). Transient-absorption spectroscopy reveals a long-lived photo-generated charge-transfer state (τ_{CR} = 6.5 μs) capable of chemical transformation under a biased voltage. Spiro-CS_2Ni can endure a compelling range of pH (1-12 for weeks) and hours of electrochemical and photoelectrochemical conditions in presence of water and organic acids. We believe this work provides crucial design principles for low-density, porous, light-energy-conversion materials.

INTRODUCTION

Exploitation of materials capable of converting solar energy to both voltaic and chemical energy have attracted extensive attention.[1-4] However, for photoelectrochemical (PEC) energy conversion, developing molecular materials that can harvest light and concurrently transport excitons as well as (generated) charge carriers have been challenging. Charge mobility in molecular assemblies is commonly improved *via* charge delocalization through high degree of chemical and electronic conjugation. Such electronic properties lower the optical bandgap of the materials and, the photosensitizer component, therefore, fails to generate charge carriers with enough potential to drive a photocatalytic reaction. Therefore, PEC developments critically need new approach for molecular materials with desired chemical and electronic properties to enable optimal diffusion of energy, charge, and chemical components (*e.g.*, substrate, reagent, counterions, and product).

Molecular assemblies provide access to synthetically tunable electronic properties through chemical alteration of the constituent building blocks. Designer materials such as porous coordination polymers (PCP)—including metal–organic frameworks (MOFs)—provide scalable and modular platforms with a high accessibility of catalyst sites if installed.[5, 6] In these materials, the molecular-scale porosity facilitates mass transport for counterions, solvent molecules and reacting species, where wide range of desired complementary functionalities can be readily installed.[7-11] Wide range of redox-active building blocks (i.e., organic linkers or struts and metal nodes) with exquisite photophysical or photochemical properties can be integrated to drive photoelectrochemical processes.[12-16]

With respect to charge transport processes, existing MOFs tend to lie on one of two extremes: *i)* "traditional" 3D MOFs (based on metal-carboxylate coordination)[17-20] that lack appropriate electronic properties required for augmented charge mobility (these materials display a conductivity of $<10^{-12}$ S/cm, unless redox active building units with matching potential are used[21]), and *ii)* emerging 2D-MOFs that display high charge mobility due to a small or zero bandgap, which compromises the potential energy of the redox equivalents.[22-30] Metal-carboxylate connectivity entails a poor orbital overlap (*i.e.*, significant energy mismatch) and low band dispersion, which results in localized metal or ligand –centered frontier orbital energy levels that significantly restrain charge migration across the material.[31, 32] Emerging exploitation of metal-sulfur or metal-nitrogen coordination in (usually) 2D structures have succeeded to lower the energy mismatch and/or achieve high degree of charge carrier density leading to a few high-conductivity MOFs, often displaying metallic behaviors.[22-28] Likewise, materials assembled from sulfur-based conjugated compounds, e.g., tetrathiofulvalene (TTF) derivatives, are also common to achieve augmented charge mobility: these includes (distorted) stacked assemblies of metal tetra-thiolate 1D chain showing metallic behavior,[33] and tetracarboxylate HOF[34] showing semiconducting behavior. Based on the above, the goal of achieving materials with optimal charge mobility with sufficient optical bandgap points to an orthogonal material design through alternative assembly chemistries to maximize usable redox equivalents for energy conversion processes.[2, 35-37]

In this work, we report the development of an intrinsic semiconducting 3D porous framework that exploits the augmented electronic connectivity of metal-carbodithioate '($—CS_2)_nM$' (Figure 1) to achieve a delocalized charge-carrier state and, thereby, a high through-bond charge mobility (relative to that in typical metal-carboxylate MOFs).[38-40] A significant degree of electronic communication can be realized through a good energy matching between the metal-centered orbitals and ($—CS_2^-$)-derived ligand-group orbitals (LGOs) involving 3p orbitals. However, the unique feature of carbodithioates that warrants the evolution of a unique composition lies on its moderate-to-strong ligand-field strength, which facilitates the generation of low-spin (LS) complexes. Therefore, ($—CS_2)_nM$ linkage chemistry is poised to provide a different set of *d*-electron configurations (through paired electrons) enabling realization of intrinsic semiconductors due to filled metal-ligand bands with tunable bandgaps. This strategy is distinct from the typical high-spin (HS) coordination systems attained in thiolate-based frameworks where unpaired electrons leading to partially filled bands (responsible for their metallic behavior). We envision that '($—CS_2)_nM$' -derived MOFs constructed from transition metal ions with even number of *d*-electrons (>5) will entail (diamagnetic) intrinsic semiconducting materials possessing electronically delocalized frontier orbitals to augment charge-carrier conductivity.[41] Yet, these materials will have sizable optoelectronic bandgaps as to enable visible light photoexcitation. Besides this fundamental design principle, it can be expected that the ligand directionality of the well-established carboxylate ($—CO_2^-$) appended struts can be translated to the carbodithioate struts. This can potentially lead to a vast library of possible ($—CS_2^-$) struts, specifically constructed with photo- and/or redox-active cores. Therefore, a wide range of 3D porous semiconducting MOFs can be realized without being limited by the stringent symmetry criteria required for the established 2D stacked frameworks.

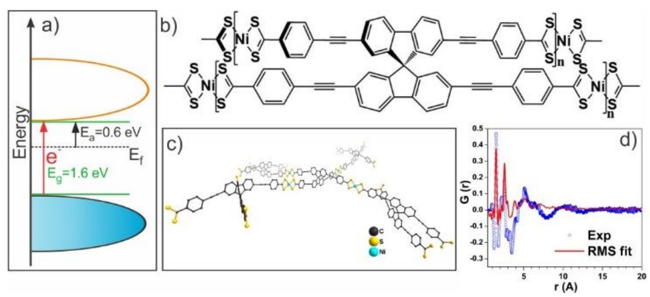

Figure 1. a) Electronic band structure of a desired intrinsic semiconducting porous material with an optical band gap suitable for visible light excitation; b) Chemical structure of Spiro-CS_2Ni; b) Representative fragment of Spiro-CS_2Ni highlighting spirobifluorene as the chromophoric core and $(-CS_2)_2$Ni as the chelating moiety; c) Experimentally collected total scattering pattern (blue) and simulated scattering pattern (red) from an approximated amorphous model obtained via a reverse Monte Carlo procedure.

With the above design principles in mind, we exploited 9,9-spirobifluorene to prepare the organic strut, which interconnected through a charge-neutral square planner '($—CS_2)_2$Ni' node generated Spiro-CS_2Ni (Figure 1). To our knowledge, this is the first 3D porous MOF built extensively with metal-carbodithioate linkage chemistry. Still, the titled Spiro-CS_2Ni assembled as a flexible amorphous material, possessing: *i)* porosity and a BET area of ~400 m^2/g (as obtained from N_2 sorption measurements at 77K of a solvent-removed 'closed pore' framework), *ii)* ≳ 90% solvent-accessible porosity of a solvent-soaked 'open pore' framework, and *iii)* a bandgap of 1.57 eV with a (semi-)conductivity $\sigma = 10^{-7}$ S/cm. These features make Spiro-CS_2Ni (and related design) a compelling platform for solution-based photo-(electro)catalytic development. Photophysical properties of this material includes excited-state manifolds with the low-energy state defined by a mixed metal -centered transition with ligand-to-metal-charge-transfer (LMCT) character (λ_{max} 635 nm), and a spirofluorene-centered transition appearing at 400 nm. Computational results suggest a significant extent of orbital mixing between the linker and the '(—CS_2)$_2$Ni' node. Transient absorption spectroscopic data collected over femto-to-microsecond timescale, revealed that the initial linker-centered excited state produces a charge-transfer (CT) state, where these photo-generated (bound) charge-carries can be harvested under a biased voltage manifesting photocurrent response. We believe that this study will provide critical design criteria to realize futuristic low-density materials with optimum yet tunable bandgap and conductivity for energy harvesting and conversion.

EXPERIMENTAL

Materials and synthesis

Details of chemical, reagents, and solvents used in the syntheses are provided in the supporting information (SI). Toluene (Tol), acetonitrile (MeCN), dichloromethane (DCM), and α,α,α-trifluoromethyl toluene (CF_3-tol) used for spectroscopic and electrochemical experiments were purchased from Sigma Aldrich and used without further purification. Preparation of the protected dithioate strut, 2,2',7,7'-tetra[2-(trimethylsilyl)ethyl dithiobenzoate-4-ethynyl] - 9,9'-spirobifluorene (TTESF), strut and relevant intermediates are described in the SI.

Spiro-CS_2Ni: TTESF (44 mg, 0.03 mmol) was dissolved in 4 mL tetrahydrofuran (THF) in a Schlenk flask under the protection of argon, to which 0.19 mL tetra-n-butylammonium fluoride solution (TBAF, 1M in THF) was added. The mixed solution was stirred at room temperature for 30 min. After that, THF was gradually evaporated at room temperature under vacuum. The solid residue was again dissolved in 5 mL chloroform affording a reddish-brown solution. A separately prepared nickel solution (dissolving 14.7 mg nickel(II) chloride hexahydrate (0.06 mmol) in 1.5mL methanol) was added drop-wise into the linker solution over the course of 20 min and the mixture was stirred at room temperature for an-other 30 min. Note that all solvents mentioned above are oxygen-free. The resulting dark green powder was washed sequentially by chloroform and methanol. Methanol was exchanged with ethanol for storage and further usage of the product (including supercritical CO_2 activation.[42])

Methods

Synchrotron total scattering data for pair-distribution function was collected at beamline 17-BM of Advanced Photon Source, Argonne National Laboratory, with an incident wavelength of 0.24153 Å. Supercritical-CO_2-dried sample was loaded into Kapton capillaries (d = 1 mm) for measurements. Scanning Electron Microscopy (SEM) images and Energy Dispersive Spectroscopic (EDS) data were collected on a Quanta FEG 450 SEM equipped with an Oxford INCA-EDS system. Electrochemical measurements for homogeneous and solid samples were performed on Autolab 128N potentiostat using a standard three-electrode cell with a platinum counter electrode, an Ag/AgCl (3 M KCl) reference electrode, and a working electrode. The preparation of working electrodes with Spiro-CS_2Ni is described in SI. Raman spectra were collected on a Princeton IsoPlane-320 Raman spectrograph equipped with PIXIS eXcelon CCD camera and interfaced with an Olympus IX-71 inverted microscope (with 20x objectives); the sample was excited with 633 nm HeNe laser. Absorption spectra for Spiro-CS_2Ni:polystyrene films was acquired using a Cary 5000 spectrometer with a diffuse reflectance accessory (DRA) in the center mount configuration; simultaneously measured transmittance (%T) and reflectance (%R) were combined (%TR) to determine absorbance (= $-\log_{10}$[%TR]). Femtosecond transient absorption (fs-TA) spectroscopic data were collected on HELIOS Ultrafast Systems. Nanosecond-transient absorption (ns-TA) measurements were performed on transient spectrometer EOS-FIRE (see SI sec B1 for details). Target analysis was performed using the Glotaran package.[43]

RESULTS and DISCUSSIONS

Synthesis and characterizations:

The synthesis of the TTESF, the ester-protected organic strut, (TTESF), was achieved through Sonogashira cross-coupling reactions between a tetra-ethynylene-appended spirobifluorene core and four equivalent iodo-dithiobenzoate-P esters. Here, P can be common silicon protecting group amenable for fluoride mediated deprotection liberating a carbodithioate salt ready for framework construction. This strategy was key to circumvent the hydrolytic instability of carbodithioic acid (particularly in common self-correcting solvothermal conditions for crystalline MOF synthesis). While this protocol defines a generality of the linker synthesis that can be translated to any organic core regardless of their symmetry, the salt-based synthesis provided a kinetically controlled synthetic condition. This bottom-up approach leads MOF that lacks much of long-range ordering.

As can be expected, with long node-connecting 'arms' (i.e., ethyne-phenyl-CS_2NiCS_2-phenyl-ethyne), Spiro-CS_2Ni entails a flexible framework that undergoes capillary-force-driven collapse/shrink (closed-pore form) upon thermal removal of the guest solvent.[44] To prevent irreversible structural damage, the solvent from a thoroughly washed Spiro-CS_2Ni sample was removed *via* supercritical CO_2 (SCO) activation. Estimated from its N_2 isotherm (Figure 2b), the resulting 'close pore' solid sample entailed a Brunauer–Emmett–Teller (BET) area of ~400 m^2/g. The thermogravimetric analysis (TGA; Figure S1b) of a solvent (DMF)-soaked Spiro-CS_2Ni showed ~90% of the initial mass loss due to solvent filling of void spaces (within the 'open pore' framework). It follows from these measurements that Spiro-CS_2Ni features a framework of extremely low-density and exceptional porosity. The 'closed pore' SCO-sample appears to transform back to original 'open pore' form when soaked in solvent (showing a similar solvent loss in TGA, hence marking reversible solvent-accessible porosity).[45, 46]

To establish the local node structure, we collected Raman spectra (Figure 2a) of the titled compound, which evinced a symmetric C-S stretching at 947 cm^{-1}, and the aromatic C—C and C_{Ph}—C_S vibrations appear at 1141 and 1271 cm^{-1}, respectively. Weak Ni-S stretching peaks can be observed in the 380 - 475 cm^{-1} (See also Figure S29). Given that $(Ph\text{-}CS_2)_2Ni$ is known,[47] we prepared a solubilized monomeric compound namely (tBu)Ph-CS_2Ni (which is a 4-tertbutyl phenyl appended $(Ph\text{-}CS_2)_2Ni$, see SI sec A4) and used it as a synthetic model to identify the vibrational bands by comparing its experimental spectrum with the computed bands (Figure S10) using density functional theory (DFT). The single C—S stretching band in the pristine solid suggests a symmetric '$(—CS_2)_2Ni$' node in Spiro-CS_2Ni. The coordinatively unsaturated *sq*-planar structure of the node, in the titled MOF, was further proved by (a) observing a split of the 947 cm^{-1} band in presence of coordinating ligand (*e.g.*, 1-methyl imidazole, MIM), and (b) 1:4 nickel:sulfur ratio obtained in SEM-EDS. The phase purity was further supported via solid state cross-polarization magic angle spinning (CP/MAS) ^{13}C NMR spectroscopy (Figure S2) which provide a broad peak for such low-density materials.[48]

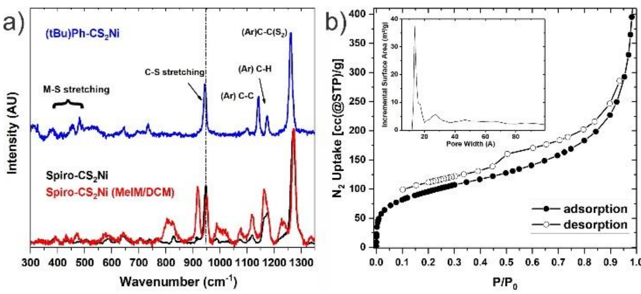

Figure 2. a) Raman spectra of Spiro-CS_2Ni with (red) and without (black) MIM axial coordination, and that of the model (tBu)Ph-CS_2Ni compound (blue) for comparison; b) Measured N_2 sorption isotherm for Spiro-CS_2Ni and extracted pore size distribution (inset).

X-ray diffraction pattern (Figure S1a) for Spiro-CS_2Ni showed a broad featureless wave, indicating the amorphous nature of the framework which lacks long-range structural periodicity. However, pair distribution function (PDF) analysis, based on total X-ray scattering, effectively enables to extract average atom−atom distances, and serve as an indication of local and intermediate ordering within amorphous solids.[49] We sought to leverage this information to generate an approximated structure of the synthesized material using reverse Monte Carlo (RMC), which is computational method that can generate plausible structural models for amorphous materials. The essence of RMC is to start with a stoichiometrically correct "guess" of the material structure, where the initial guess is continuously evolved through random structural changes such as the translation or rotation of atoms/molecules/fragments. These continuously proposed changes are accepted with probability P:

$$P = \min\left(1, e^{-\lambda^2/2}\right) \qquad (1)$$

where λ quantifies the difference between a structure-dependent measurable property for the material and the calculated value of this property for the model. In our case:

$$\lambda = \sum_i \frac{(G_{obs}(r_i))^2 - \left(G_{sim}(r_i)\right)^2}{\sigma} \qquad (2)$$

where $G_{obs}(r_i)$ and $G_{sim}(r_i)$ are observed and calculated pair distribution values for the material and the model, respectively, at discrete values of pair distance r_i ranging from 0 to 25 Å. Importantly, while RMC-generated models are neither "unique," "true" or "correct," these models can greatly aid one's understanding of a material structure.[50]

As we found that RMC had limited ability to evolve initial guesses of Spiro-CS_2Ni—primarily due to the large-aspect of ratio of the "spiro" strut (and strict coordination rules)—we sought to aid the RMC procedure by providing multiple initial guesses for Spiro-CS_2Ni using our code ToBaCCo-3.0 (see SI section B2), whose "top-down" construction algorithm is detailed elsewhere.[51] Essential to the code is the use of a chemistry-agnostic network "templates" (a Euclidian space-embedded graph) onto which chemical building blocks are ultimately mapped. Note that while the original intent for ToBaCCo is to use periodic ordered templates, here we developed a procedure to generate periodic pseudo-amorphous (PPA) templates. To generate these templates, we initialized simulation boxes with N randomly inserted "points" and stochastically evolved their positions. Here the goal was to evolve the positions such that they end up being consistent with a 4-connected network template featuring square-planar symmetry nodes. The evolution was carried out in accordance with the well-known Metropolis-Hasting Monte Carlo acceptance rules (analogous to Eq. 1). For use with these rules, each configuration of points had a pseudo-energy calculated, which used harmonic potentials to penalize deviations from the targeted network features (see details in SI).

Each generated PPA template was rescaled by ToBaCCo and the Spiro-CS_2Ni building blocks (see Figure S3) were mapped onto it to generate an atomistically detailed structure. The geometry of each structure was then optimized by minimizing its energy (at T = 0 K), with this energy being expressed as a function of atom positions according to the UFF4MOF force field. Each structure was further modified via molecular dynamics in the NPT ensemble at T = 298 K, with the final structure used as input for RMC "refinement." The RMC procedure was constrained to maintain bonds, angles, and dihedrals to stay within 1% of the input values, using an adjustable scale factor that could vary from 0.1 to 1.0. The structure most consistent with the experimental G(r) (Figure 1d) confirms a 3D framework (Figures 1c, S4), which entails C-C distances of 1.5. 2.3, 2.6, and 3.0 Å; various C-S distances ranging from 1.8-4.2 Å, various M-S distances of 2.45 Å, and distances between the closest Ni-centers or Spiro-struts ranging between 6.8 and 9.7 Å and 8.8-9.22 Å, respectively. In consistency with experimental porosity measurements, these data suggest that the solvent-removed (shrunk) form of Spiro-CS_2Ni is porous and contains non-stacked subunits. Additionally, the RMC-refined model is consistent with the local environment around Ni sites to be (at least most commonly) described by the envisioned Ni-S coordination geometry presented in Figure 1b.

Electrochemical properties:

Modified fluorine-doped tin oxide (FTO) and glassy carbon (GC) working electrodes—prepared by depositing Spiro-CS_2Ni *via* electrophoretic deposition (EPD) or drop casting on the clean electrode surface (see SI section B2)—were used to investigate various electrochemical properties. Cyclic voltammetry (CV) scan showed characteristic redox peaks at *ca* -0.75 V, -1.3 V (gap ~ 550 mV), and at +1.5 V (vs Ag/AgCl; Figure 3a). The electrochemical bandgap of 1.57

eV was determined from the onset potentials of the first redox waves. The redox potentials of -1.41V and +1.67V measured for the Spiro-CS_2P linker (dissolved in DCM solvent) indicate that the redox events at -1.3V and +1.51V for Spiro-CS_2Ni are mostly ligand-derived, but lower in energy due to electronic communication established through the metal coordination in the framework. Thus, the peak appearing at -0.75 V is for '(—CS_2)$_2$Ni' –centered redox event. The impact of the electronic mixing and the extent of electronic delocalization in the framework can be realized by comparing the potentials relative to the (*t*Bu)Ph-CS_2Ni model compound. The metal-centered reduction displayed ~60 mV anodic shifts and the oxidation event manifested ~170 mV cathodic shifts (Figure 3a). The irreversible redox peaks in the CV are commonly seen for MOF samples that are not directly grown on the electrode surface (i.e., working electrodes that are made *via* post-synthetic deposition).[52] These do not necessarily indicate a poor material stability or chemical degradation of the charged materials as Raman spectra collected for films after three hours of electrolysis showed negligible change of peaks compared with the fresh sample (Figure S9).

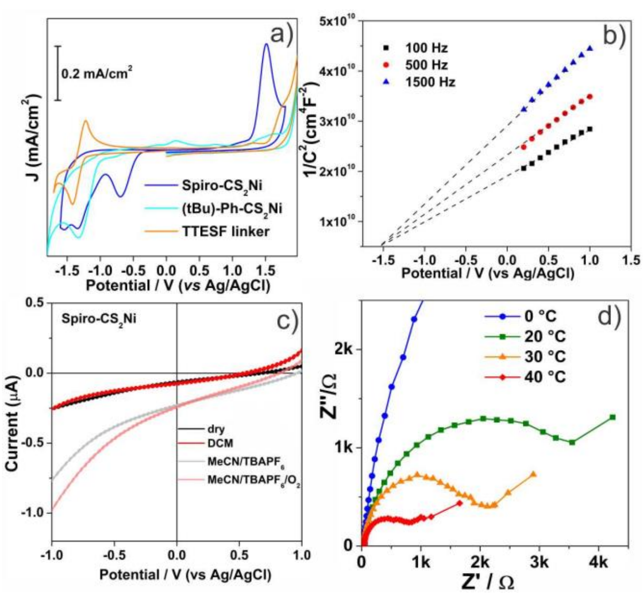

Figure 3. a) CV scans of Spiro-CS_2Ni deposited on FTO glass electrode, (tBu)Ph-CS_2Ni, and TTESF/Spiro-CS_2P linker collected in DMF solvent; b) Mott–Schottky plots of Spiro-CS_2Ni collected at multiple frequency; c) I-V curve of Spiro-CS_2Ni measured in different conditions; d) Temperature dependent alternating current impedance spectra of Spiro-CS_2Ni.

Conductivity measurements

Impedance spectroscopic measurements of Spiro-CS_2Ni (EPD on FTO in 1M $TBAPF_6$ in acetonitrile) revealed a charge-carrier conductivity of 0.95×10^{-8} S/cm and 1.1×10^{-7} S/cm at respective bias voltages of -0.75 V and -1.3 V.[53] The conductivity determined from the ohmic current (I_d) measurement with a film (8 μm) deposited over platinum interdigitated electrode (IDE; two sets of 250 Pt-fingers working electrodes with 5 μm gap; $I_d = (i_1-i_2)/2$) at 10 mV potential difference corroborates well with the impedance data (Figure S6). Impedance spectroscopic data collected as a function of temperature (Figure 3d) also suggest a semiconducting behavior: σ (at -1.3 V) = 6.4×10^{-8} S/cm, 1.1×10^{-7} S/cm, 6.4×10^{-7} S/cm, and 1.9×10^{-6} S/cm was recorded at 0, 20, 30, and 40 °C, respectively. The Arrhenius analysis, obtained from the linear correlation between ln(ρ) and 1/T (0 to 40 °C) provided an activation energy (E_a) of 0.62 eV (Figure S7c).[54] Furthermore, positive slopes of linear Mott-Schottky plots ($1/C^2$ *vs* potential; Figure 3b) reveals that Spiro-CS_2Ni is an *n*-type semiconductor material, with a flat-band potential is of -1.53 V (vs Ag/AgCl). The impact of the flexible framework conformations—an open (solvent-soaked) or close pore (solvent removed)—was probed via recording the current-potential (I-V) curves for respective films.[55] The corresponding sigmoidal I-V curves (Figure 3c), collected with a dried and solvent (DCM)-soaked films did not evince any sizable difference. However, improved current (higher slope in the I-V curve) was observed with increase in solvent dielectrics and presence of molecular oxygen in the media. Improved conductivity in air saturated media may be due to O_2 binding to the metal center (the corresponding CV displayed a peak shift for the metal-centered reduction; Figure S7) points towards potential small molecule binding and concurrent activation.

Impact of axial coordination: Inspired by these results, we wanted to further explore the impact of substrate binding as mimicked via axial coordination (to the coordinatively unsaturated sq-planner 'Ni' sites) in electrochemical properties. The *d*-electron configuration and therefore the spin state and energy are function of coordination environment and its symmetry. Therefore, in a coordinatively unsaturated *sq*-planar complex, incorporation of an axial coordination can be an effective strategy to perturb ligand-field splitting energy and symmetry,[56-59] which we have shown in metalloporphyrin based MOFs to improve charge transport[60] and was successfully adopted in subsequent electrocatalytic activities.[61] For Spiro-CS_2Ni, we exploited MIM (10 mM in the electrolyte solution) to coordinate to the square planar '(—CS_2)$_2$Ni' node. The Raman spectrum recorded for Spiro-CS_2Ni in presence of MIM showed new peaks at 987-1028 cm^{-1} (broad), 917cm^{-1}, and 804 cm^{-1} that can be assigned to Ni-N bending, C-N stretching and bending of MIM, respectively (Figure 2a). However, the extent of such coordination should be limited to avoid condition enforcing significant ligand exchange (replacement of the carbodithioates was observed by >50 mM MIM) causing structural damage of the solid (see Figure S11 for a DFT-calculated cluster model).[62] At low MIM concentration, a five-coordinated square pyramidal ligand-field can be conceived where the N_{MIM} occupies the apex position of Ni-S_4 square base.

The electrochemical properties of SpiroCS_2-Ni-MIM are highlighted by the anodic shift of the first, node-centric, reduction potential and a cathodic shift of the ligand-centered second reduction peak (from -1.38 V to -1.46 V) with a higher current density due to improved conductivity (Figure S8a). The impedance spectroscopic data suggest *ca* 30-fold boost in the conductivity in the presence of 10 mM MIM (Figure S8b). The Arrhenius analysis of the temperature-dependent conductivity at -1.3 V suggest that a significant lowering of the activation energy (E_a = 0.13 eV) in a modified coordination environment is the reason behind such improved charge-carrier conductivity (Figure S8d).

Mechanistic investigation of electron transport

The charge transport properties in such semiconducting materials can be described as $\sigma = \mu \bullet \nu$, where ν is the charge carrier density and μ is carrier mobility. The latter can be a function of the extent of electronic delocalization. For band-like transport, μ is inversely proportional to the effective mass (m^*) of the carrier. A small m^* can be achieved via augmented orbital overlap, which in Spiro-CS_2Ni can be achieved through metal-carbodithioate linkages. On a single molecular basis (i.e., a monomeric model), factors like the *d*-electron energy and configuration—as a function of its coordination geometry—can be perceived to define the underlying electronic structure (see SI sec F). Computing the electronic properties in an extended solid polymeric structure would be extremely difficult for a non-periodic system due to the large number of atoms that would be involved in such computation. Thus, to elucidate how the electronic properties perceived in a monomeric system transform to the band structure (with an isotropic dispersion for amorphous frameworks) of the polymeric framework, we postulated that an 'idealized' crystalline model structure with non-aggregated units and comparable density and hence, presumably, similar inter-unit space would serve a reasonable picture of the electronic properties of Spiro-CS_2Ni. Such idealized approach has been successfully adopted in stacked 1D polymeric TTF system.[33]

For this, we used ToBaCCo to generate several crystalline structures in different topologies, including *cdm*, *nbo, rhp*, *zea*, *sql*, and a catenated-*sql* (*c-sql*) nets (see Figure S5 for a few examples). Among these, the *c-sql* structure was chosen as it possesses a comparable solvent-accessible void space (and thus presumably a through-space strut-strut separation distances) to the synthetized Spiro-CS_2Ni sample.[63] The partial density of state (PDOS) diagram (Figure 4a; also see SI sec F2) was constructed via periodic DFT calculations using the PBE-U functional (U correction = 6 for p-orbital of S and 9 for the d-orbital of Ni) and a plane-wave basis set. This calculation predicts a bandgap of 1.55 eV for the model—close to the measured electrochemical (1.57 eV) and optical (1.60 eV; *vide infra*) bandgaps.

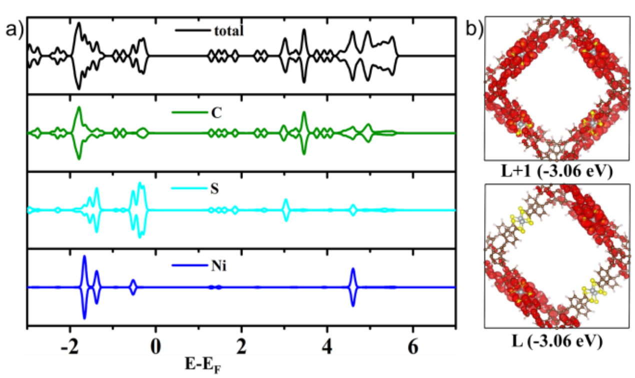

Figure 4. a) Total and partial DOS, and b) LUCO (L) and LUCO+1 (L+1) with (PBE-U energy) for an idealized crystalline (catenated-sql net) computational model.

The PDOS diagram suggests the contribution of both metal and ligand-centered orbitals in the total DOS. The electron density plots suggest that the lowest unoccupied crystal orbital (LUCO) is mixed, but more of a '(—CS_2)$_2$Ni' –contributed. On the contrary, the LUCO+1 is significantly dispersed (Figure 4b). This computational result is consistent with the initial prediction and experimental data on the conductivity values measured for the first and the second reduction potential (the band structure or electronic dispersion obtained from the crystalline model would be irrelevant for our amorphous isotropic system).

The above data suggest intuitive design rules for porous semiconducting materials with through-bond conductivity. For example, a strong-field carbodithioate forming *sq*-planer LS d^8 '(—CS_2)$_2$Ni' –based 3D porous MOF that requires charge doping to measure conductivity. Therefore, electrode-injected charge during the reduction event comes with a balancing counter ion, which can impede the charge mobility. Furthermore, at the bias potential of the first reduction, a node localized LUCO entails a lower conductivity than the one measured at (more delocalized) second reduction potential. It will be intriguing to see if a degenerate LUCO and LUCO+1 (or small gap) can provide opportunities for electronic mixing improving their charge conductivity.

Photophysical properties:

Electronic transitions: Electronic absorptive transitions for Spiro-CS_2Ni were analyzed relative to the TTESF linker as well as experimental and small-scale computational models (Figure 5; SI sec F1). The TTESF linker exhibits a weak low-energy CS_2-centered $n \longrightarrow \pi^*$ transition at 502 nm, and an intense aromatic $\pi \longrightarrow \pi^*$ transition at 390 nm (Figure 5, blue spectrum). The broad, yet distinct, electronic transitions for the Spiro-CS_2Ni (polystyrene film) appear at 370 nm, 450 nm, and the low-energy one centering at 580 nm that extends up to 775 nm (optical bandgap =1.60 eV; see table S1 for comparison with relevant literature compositions). The experimental absorption spectrum of (tBu)Ph-CS_2Ni (DMF solution) highlights a low energy manifold spanning *ca* 580-750 nm. This consisted of a weak *d-d* transition that appears red to 650 nm and two relatively more intense *d-d* transitions appearing at 635 and 595 nm, respectively. The sizable oscillator strength (*i.e.*, compared to a typical *d-d* transition) of the latter bands indicates strong ligand-metal electronic mixing and may have charge-transfer (CT) character (Figure 5).[47]

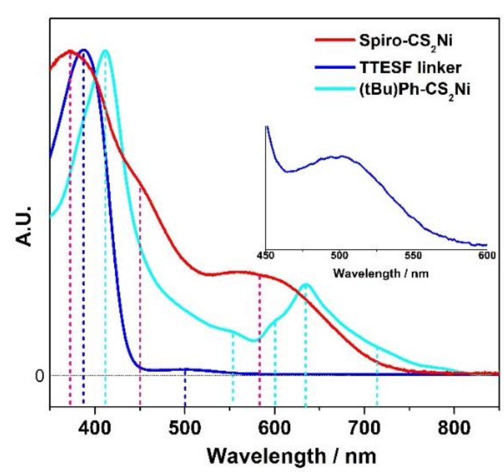

Figure 5. Absorption spectra of Spiro-CS_2Ni (polystyrene film), Spiro-CS_2P linker (DCM) and t(Bu)Ph-CS_2Ni (DMF) model compound [inset: a magnified spectrum showing the 500 nm transition of TTESF linker]

Non-periodic, standard DFT and time-dependent DFT (TDDFT) calculations with a hybrid functional and localized basis set (PBE0/6-31g(d,p)) on a (*t*Bu)Ph-CS_2Ni model (Figures S12, S13) reveal a weak low energy transition at 644 nm and a more intense band appearing at 547 nm. Natural transition orbital (NTO) analysis[64] for these transitions (Figure S13b) suggest that the weak 644 nm transition involves both *d*-*p* and partially CT character (a NiS_4 centered NTO with Ni 3*d* ⟶ a metal-ligand mixed NTO involving Ni 4p_z), whereas the 547 nm transition involves significantly more mixed NTOs (involving Ni 3*d* to Ni 4p_z). These relatively intense (Laporte relaxed) transitions can be attributed to stemming from $g \longrightarrow u$ symmetric NTOs achieved through a good metal-ligand orbital mixing. In contrast, the higher energy transitions at 421 nm involves more delocalized (ligand derived) NTOs (also with noticeable extent of metal orbital mixing involving $g \leftrightarrow u$ symmetric NTOs). A DFT//TDDFT computation (PBE0/6-31g(d,p) level theory; a different basis, such as def2-TZVP, overestimates the transition energies; with similar NTOs; see Figure S18) on a truncated model, Spiro-CS_2Ni-*m* (constructed from a single monomeric Spiro strut where each of the four '(—CS_2)$_2$Ni' node is terminated with a Ph-ethyne-Ph-CS_2 moiety; Figure S14-S17) manifest similar NTOs involvement for the low-energy weak transition at 650 nm (Figure S17b) and a relatively more intense one at 565 nm (Figure S17c). The higher energy transitions involve NTOs that are significantly spiro- and/or its organic arm -derived $\pi \longrightarrow \pi^*$ type (albeit, mixed with some degree of metal orbital) but with more; Figure S17d, e). Nevertheless, all the involved NTOs highlight different extent of metal-linker electronic mixing including extended delocalization availed through the ethyne-bridged strut design. Such a high degree of metal—linker orbital mixing can be beneficial for the through-bond charge mobility.

Excited state dynamics: Given the excited states involving various mixed and CT characteristics, we wanted to probe the corresponding dynamical processes. Congruent with this assessment, SpiroCS_2-Ni composition is non-emissive for the entire excitation range (λ_{ex} = 380-600 nm), possibly due to the involvement of a low-energy CT state, which facilitates a nonradiative-decay of the initially prepared (polar) excited state. Femto-second transient absorption (fs-TA) spectroscopic data collected for Spiro-CS_2Ni suspension in toluene solvent (Figure 6a; λ_{ex} = 355 nm) display ground state bleaching (GSB) band <450 nm and a broad excited-state absorption (ESA) in the 625-730 nm region. Within this ultrafast time domain, global fitting suggests a single-component exponential-decay with τ =1.9 ns, for ^{1}S state of Spiro-CS_2Ni.

With such a "monotonous" fs-TA profile, we wanted to probe the complexity of its excited state dynamics and possible evolution of long-lived states in the expanded nanosecond -microsecond time domain. Spiro-CS_2Ni, suspended in deaerated toluene, evinced a characteristic ESA band centered at 690 nm (Figure 6b) with a lifetime of a few nanoseconds; these features are reminiscent to the ESA band seen in fs-TA spectra (Figure 6a). This short-lived initial singlet species appeared to decay to a long-lived (μs) state that does not appear to manifest any ESA, only a GSB at 470 nm (Figure 6b) tailing beyond 700 nm.

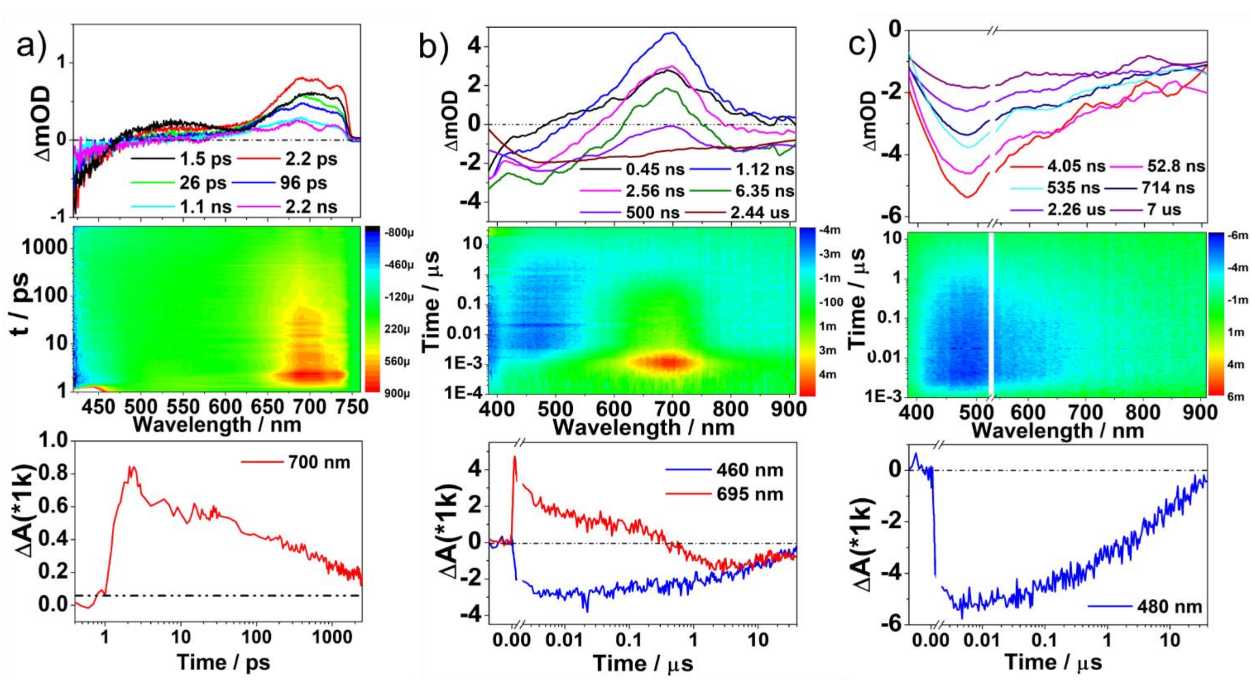

Figure 6. a) Fs-TA and b) ns-TA spectra of Spiro-CS_2Ni collected in toluene, λ_{ex} = 355 nm; c) ns-TA spectra of Spiro-CS_2Ni in toluene, λ_{ex} = 532 nm. Each spectral set includes three panels, top: time-resolved transient absorption spectra at different pump-probe delay time; middle: 2D pseudo-color mapping of TA-spectra of Spiro-CS_2Ni; bottom: kinetic traces at probed wavelength.

Global fitting (parallel decay) of this ns-TA data reveals two species with 4 ns and 6 μs time constants. These spectral features as well as the corresponding time constants did not appear to be impacted by the presence of molecular oxygen, which indicates that the long-lived species may not be a triplet. In contrast, the ns-TA spectra of the TTESF linker (λ_{ex}=335 nm, in deaerated toluene) evinced a 450 to 850 nm broad ($S_1 \longrightarrow S_n$) ESA band peaking at 650 nm, this band decays with k = (3.9 ns)$^{-1}$ and evolves to a long-lived species with ESA at ~600 nm possibly corresponding to its $T_1 \longrightarrow T_n$ transition (with τ = 2.1 μs; Figure S22).

These data suggest that the excited-state evolution for the Spiro-CS_2Ni differs significantly compared to the solution-dissolved molecular strut (Figure S22b) in a way that the initially created singlet excited state (λ_{ex} = 335 nm) decays to a low-energy singlet state bypassing the $S_1 \longrightarrow T_1$ intersystem crossing (since the long-lived state in Spiro-CS_2Ni is not O_2 sensitive nor the corresponding $T_1 \longrightarrow T_n$ ESA is visible; Figure 6b). We assign this low-energy singlet state as the CT state, which can be accessed via a high-energy (spirofluorene –centered) excitation. To understand the evolution and the dynamics of this low-energy state, we excited Spiro-CS_2Ni at a lower energy—i.e., at the mixed metal-centered *d-d* manifold (λ_{ex} = 532 nm); the corresponding ns-TA spectra (Figure 6c) evince a clear dynamics of this low energy state without evolution of the early ESA (690 nm) band that was seen during a higher energy excitation at 355 nm. The entire spectral feature of this low-energy excited state is highlighted by a broad GSB band peaking at 470 nm that recovers with k = (7 μs)$^{-1}$. One key aspect of this low-energy CT state is that it takes a few ns (3-4 ns; IRF ≲ 1 ns) evolution/rising time for both the excitation wavelengths (Figure 6b,c bottom panel). Recall that Spiro-CS_2Ni possess three major absorptive manifolds peaking at 380, 470 nm, and a broad absorption centering at 600 nm; of which, the 380 nm one was mostly a spirofluorene-derived π-π* transition and the other two involve relatively more mixed states with varying extent of Ni *d-d, d-p,* and M-L mixed characters. This photo-induced CT-state could therefore be attributed to a low-energy LMCT state consistent with the NTO analysis and electrochemical data (see the text below Figure S18). Given that the ns-TA data shown in Figure-6c only evince GSB from 470 nm extending to 800 nm, we reason that the spirofluorene centric excitation is a higher energy manifold, which shows GSB at ~380 nm (Figure 6a,b) at the earlier time[65] and then diminishes to form the new state defined by the 470 nm GSB. Therefore, organic strut with larger $\pi \longrightarrow \pi^*$ optical bandgap can be used to harvest higher energy photons, which can be efficiently transferred its energy to the lower energy manifold eventually forming a CT state.

Global fitting of the 355 nm excitation ns-TA data with a two-species A ⟶ B ⟶ gs sequential model (see SI sec B1) reveals the species-associated spectra (SAS; Figure 7): species A (τ = 4.6 ns) for the early species and B (τ = 6.5 μs) as the low-energy long-lived species.[66] The nature of the long-lived excited state was further probed as a function of solvent dielectrics: ns-TA spectra (λ_{ex} = 355 nm) of SpiroCS_2-Ni collected in CF_3Tol solvent (ϵ = 9.2; Figure S24) evince the ESA, now appearing at 780 nm (0.2 eV red shifted compared to that observed in toluene; ϵ = 2.4) and decays with a faster rate (τ= 2.0 ns). The long-lived state (τ = 6.1 μs) also showed ~0.16 eV red shift. These solvent dielectric dependent evolution and energy of the long-lived excited state are congruent with its CT nature.[67]

Given a long-lived CT state achieved through a wide range of photonic excitation (UV-vis), we wanted to probe their utility. To detect whether free charge carriers were formed after photoexcitation, flash-photolysis time-resolved microwave conductivity (TRMC) measurements were performed on Spiro-CS_2Ni:polystyrene films (see SI sec H). No appreciable photoconductivity was observed in these films when compared to the minimum detectable change in photoconductivity based on measurements of neat polystyrene control films. This indicates that the photo-generated charge carriers are either strongly held through an appreciable Coulomb binding energy and/or energetically trapped. From the electrochemical data, we can anticipate that electrons residing at the '(—CS_2)$_2$Ni' center would require a large activation energy (>0.62 eV; see electrochemistry section and Figure S8c) to be driven. Such CT states are more common in organic materials (of low dielectric constant with no sizable thermodynamic driving force to split into free carriers) and can be harvested under a bias voltage, such as those used in a photoelectrochemical setup.

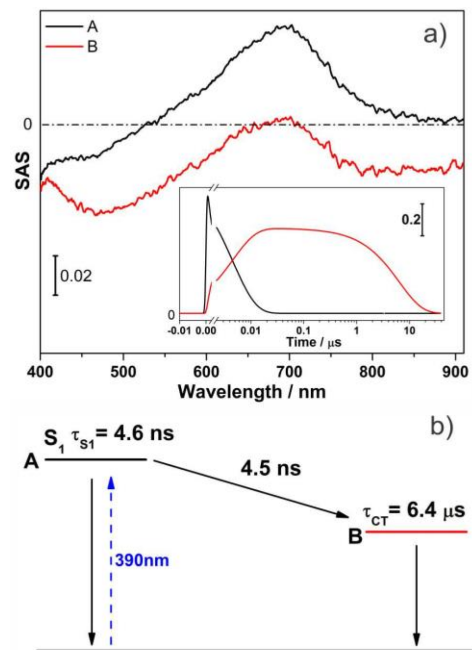

Figure 7. a) SAS spectra of Spiro-CS_2Ni ns-TA data (λ_{ex} = 355 nm) collected in toluene, inset is the state associated population evolution; b) States evolution and lifetimes of Spiro-CS_2Ni obtained from results of target model applied on ns-TA data collected in toluene.

In a proof-of-principle test whether these photo-generated charge carriers can be exploited, a Spiro-CS_2Ni@FTO (*vide supra*) was used as the photo cathode (WE) in a photoelectrochemical setup (with a Pt counter electrode and Ag/AgCl ref electrode; electrolyte = 1M $TBAPF_6$ in acetonitrile). In a chronoamperometric (CA) experiment, this WE was used to measure the transient photocurrent for proton (0.2 M acetic acid) as electron acceptor (i.e., in a hydrogen evolution reaction—HER—set up) under the excitation of 400 nm (5 mW/cm^2; Figure 8a) at -0.2 V bias voltage.[68] Current density recorded under chopped illumination revealed an immediate cathodic photo-current response reaching *ca* 5 μA cm^{-2} under the illumination of 400 nm (5 mW/cm^2) excitation. A similar low-energy excitation at 520 nm (Figure 8b) evinced a diminished photo response with a smaller photocurrent density of *ca* 2 μA cm^{-2}. This observation indicates both transitions can yield harvestable charges, and the photocurrent is consistent with the lower oscillator strength of low-energy transition (node-centered manifold) relative to the higher energy π→π* transition. The transient photocurrent response profile (i.e., shape of current waves) appears to be a function of excitation wavelength: photocurrent measured at 400 nm underscores a subsequent decay right after the rise of current, resulting in the sharp tip on the current wave, which suggests partial recombination of photoinduced electrons and holes right after excitation. However, such a rapid recombination was absent for 520 nm illumination which evinced a rise and relatively flat-head current wave. This is due to the faster recombination of high-energy photoinduced electrons with holes (i.e., excited electrons lying in higher excited states lead to higher charge transfer driving force), the minor charge carrier, trapped at the electrode surface.[69] The Spiro-CS_2Ni solid endures a wide range of dielectric media including aqueous acid (pH = 2) and base (pH = 12; see SI sec I) –which provides a promising platform for energy related developments.[70]

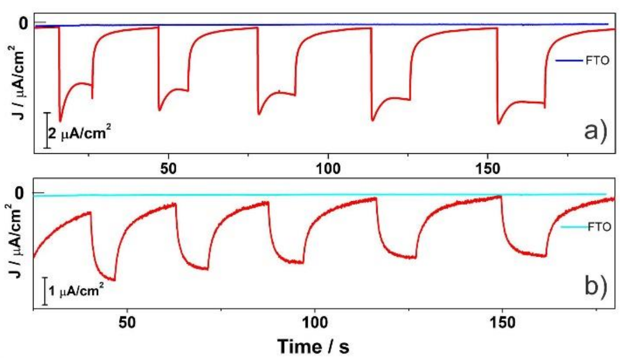

Figure 8. Photocurrent response of Spiro-CS_2Ni@FTO recorded at -0.2 V (vs. Ag/AgCl) under the illumination of a) 400 nm and b) 520 nm (5 mW/cm^2) in presence of proton as an acceptor. Corresponding baseline current density measured with a blank FTO as WE are plotted in blue (at 400 nm, panel a) and cyan (520 nm, panel b).

CONCLUSION

In this work, we have designed and constructed a robust 3D porous semiconducting MOF, Spiro-CS_2Ni, from carbodithioate-appended spirobifluorene struts to entail electronically delocalized crystal orbitals. Such electronic properties provided enhanced charge carrier conductivity (relative to those seen for common carboxylate derived MOFs) – yet preserving an optical bandgap of *ca* 1.6 eV to enable light-harvesting in a wide range of the visible spectrum. The Spiro-CS_2Ni possesses a flexible 3D amorphous framework with a BET area of ~400 m^2/g (determined from N_2 isotherm measured for a solvent-removed close-pore sample) and 90% solvent-accessible porosity for solvent-soaked 'open pore' form. The structures were modeled *in-silico*, where the initial structure was constructed using the ToBaCCo code and refined using reverse Monte Carlo simulations supported the long-range amorphous character of Spiro-CS_2Ni, whereas DFT computations on small and crystalline models suggest the electronic properties of Spiro-CS_2Ni to be largely predictable based on local structure around the MOF nodes. Being a softer base, carbodithioate linkage offers enhanced covalent character for heavier transition metal ions at their low oxidation state with better metal-ligand orbital energy match through involvement of the S-3p orbitals. This augmented electronic communication leads to unique electronic properties, including a relatively strong ligand-field strength, that generate low-spin $(\text{—}CS_2)_nM$ complexes useful to realize intrinsic semiconducting porous materials. Spiro-CS_2Ni possesses an electrochemical bandgap of 1.57 eV and an *n*-type semiconductivity of $\sigma = 10^{-7}$ S/cm at -1.3 V bias (vs Ag/AgCl) with thermal activation energy of 0.62 eV. Consistent with stronger coordination (by soft S to metal ions at their low-oxidation state), Spiro-CS_2Ni was found to be stable under hours of electrochemical reducing conditions while it can endure a wide pH range (2-12). Controlled axial coordination by imidazole ligands was found to improve electron conductivity by 30-fold, possibly through lowering the activation energy (E_a) down to 0.13 eV (via alteration of the d-electron configuration).

The electronic excitation of Spiro-CS_2Ni revealed some unique features defined by the various degrees of metal-strut electronic mixing evolving a low-energy intense *d-d* transition manifold and two others at 470 nm and 380 nm. The latter one is defined by a more spirofluorene derived (π→π* type) transition. TDDFT computation and subsequent NTO analyses on small model structures suggest that the *d-d* transitions involve metal 3d-derived orbitals to a $4p_z$-derived one, with various extents of π-conjugation from the strut (resulting a panchromatic absorption). Femto-microsecond transient spectroscopic data indicate a short-lived (τ = 4.6 ns) strut-centered singlet state achieved through high-energy (355-400 nm) excitation, which can then populate a relatively low-lying long-lived singlet CT state (τ = 6.5 μs) characterized by bound charged that can be effectively harvested for HER (at -0.2V). Altogether, the result delineates design principles for low-density semiconducting 3D MOFs for light-harvesting and energy conversion.

ASSOCIATED CONTENT

Supporting Information. Experimental details, additional computational and spectroscopic data. This material is available free of charge via the Internet at http://pubs.acs.org.

AUTHOR INFORMATION

Corresponding Author

* Pravas Deria
pderia@siu.edu.
* Diego A. Gómez-Gualdrón
dgomezgualdron@mines.edu

ACKNOWLEDGMENT

This work was seeded by Ralph E. Powe Junior Faculty Enhancement Award, administered by ORAU and partly supported by the SIU Advanced Energy Institute (through the Advanced Energy Resource Board). P.D. acknowledges the National Science Foundation (NSF CAREER CHE-1944903) for partial support. D.A.G.-G. acknowledges support from NSF CAREER Award (CBET 1846707) and computational resources from Colorado School of Mines (Mio Supercomputer). Use of the Center for Nanoscale Materials as well as of Beamline 17-BM of the Advanced Photon Source, Office of Science user facilities, were supported by the U.S. Department of Energy (DOE), Office of Science, Office of Basic Energy Sciences, under Contract No. DE-AC02-06CH11357. S.M.P. and C.J.C. acknowledge the computational facility supported by the DOE, Basic Energy Sciences, Division of Chemical Sciences, Geosciences and Biosciences under Award DE-FG02-17ER16362. SEM-EDS data were collected at the SIUC IMAGE center (supported by NSF grant CHE-0959568). T.G.A. and G.R. acknowledge funding for absorption spectroscopy and TRMC measurements provided by the U.S. DOE, Office of Science, Office of Basic Energy Sciences, Solar Photochemistry Program, to National Renewable Energy Laboratory under Contract No. DE-AC36-08GO28308.

REFERENCES

(1) Barber, J.; Andersson, B. Revealing the Blueprint of Photosynthesis. *Nature* **1994**, *370*, 31-34.

(2) Wasielewski, M. R. Self-Assembly Strategies for Integrating Light Harvesting and Charge Separation in Artificial Photosynthetic Systems. *Acc. Chem. Res.* **2009**, *42*, 1910-1921.

(3) Sengupta, S.; Würthner, F. Chlorophyll J-Aggregates: From Bioinspired Dye Stacks to Nanotubes, Liquid Crystals, and Biosupramolecular Electronics. *Acc. Chem. Res.* **2013**, *46*, 2498-2512.

(4) Miller, R. A.; Presley, A. D.; Francis, M. B. Self-Assembling Light-Harvesting Systems from Synthetically Modified Tobacco Mosaic Virus Coat Proteins. *J. Am. Chem. Soc.* **2007**, *129*, 3104-3109.

(5) Li, X.; Surendran Rajasree, S.; Yu, J.; Deria, P. The Role of Photoinduced Charge Transfer for Photocatalysis, Photoelectrocatalysis and Luminescence Sensing in Metal–Organic Frameworks. *Dalton Trans.* **2020**, *49*, 12892-12917.

(6) Yu, J.; Li, X.; Deria, P. Light-Harvesting in Porous Crystalline Compositions: Where We Stand Towards Robust Metal–Organic Frameworks. *ACS Sustainable Chem. Eng.* **2019**, *7*, 1841-1854.

(7) Li, X.; Yu, J.; Lu, Z.; Duan, J.; Fry, H. C.; Gosztola, D. J.; Maindan, K.; Surendran Rajasree, S.; Deria, P. Photoinduced Charge Transfer with a Small Driving Force Facilitated by Exciplex-like Complex Formation in Metal–Organic Frameworks. *J. Am. Chem. Soc.* **2021**, *143*, 15286-15297.

(8) Van Wyk, A.; Smith, T.; Park, J.; Deria, P. Charge-Transfer within Zr-Based Metal–Organic Frameworks: The Role of Polar Node. *J. Am. Chem. Soc.* **2018**, *140*, 2756-2760.

(9) Goswami, S.; Yu, J.; Deria, P.; Hupp, J. T. Light Harvesting "Antenna" Behavior in NU-1000. *ACS Energy Lett.* **2021**, *6*, 848-853.

(10) Williams, D. E.; Dolgopolova, E. A.; Godfrey, D. C.; Ermolaeva, E. D.; Pellechia, P. J.; Greytak, A. B.; Smith, M. D.; Avdoshenko, S. M.; Popov, A. A.; Shustova, N. B. Fulleretic Well-Defined Scaffolds: Donor–Fullerene Alignment Through Metal Coordination and Its Effect on Photophysics. *Angew. Chem. Int. Ed.* **2016**, *55*, 9070-9074.

(11) Kuciauskas, D.; Lin, S.; Seely, G. R.; Moore, A. L.; Moore, T. A.; Gust, D.; Drovetskaya, T.; Reed, C. A.; Boyd, P. D. W. Energy and Photoinduced Electron Transfer in Porphyrin–Fullerene Dyads. *The Journal of Physical Chemistry* **1996**, *100*, 15926-15932.

(12) Feng, D.; Gu, Z.-Y.; Li, J.-R.; Jiang, H.-L.; Wei, Z.; Zhou, H.-C. Zirconium-Metalloporphyrin PCN-222: Mesoporous Metal–Organic Frameworks with Ultrahigh Stability as Biomimetic Catalysts. *Angew. Chem. Int. Ed.* **2012**, *51*, 10307-10310.

(13) Morris, W.; Volosskiy, B.; Demir, S.; Gándara, F.; McGrier, P. L.; Furukawa, H.; Cascio, D.; Stoddart, J. F.; Yaghi, O. M. Synthesis, Structure, and Metalation of Two New Highly Porous Zirconium Metal–Organic Frameworks. *Inorg. Chem.* **2012**, *51*, 6443-6445.

(14) Park, H. J.; Jang, J. K.; Kim, S.-Y.; Ha, J.-W.; Moon, D.; Kang, I.-N.; Bae, Y.-S.; Kim, S.; Hwang, D.-H. Synthesis of a Zr-Based Metal–Organic Framework with Spirobifluorenetetrabenzoic Acid for the Effective Removal of Nerve Agent Simulants. *Inorg. Chem.* **2017**, *56*, 12098-12101.

(15) Li, K.; Zhang, L.-Y.; Yan, C.; Wei, S.-C.; Pan, M.; Zhang, L.; Su, C.-Y. Stepwise Assembly of $Pd_6(RuL_3)_8$ Nanoscale Rhombododecahedral Metal–Organic Cages via Metalloligand Strategy for Guest Trapping and Protection. *J. Am. Chem. Soc.* **2014**, *136*, 4456-4459.

(16) Mondloch, J. E.; Bury, W.; Fairen-Jimenez, D.; Kwon, S.; DeMarco, E. J.; Weston, M. H.; Sarjeant, A. A.; Nguyen, S. T.; Stair, P. C.; Snurr, R. Q.; Farha, O. K.; Hupp, J. T. Vapor-Phase Metalation by Atomic Layer Deposition in a Metal–Organic Framework. *J. Am. Chem. Soc.* **2013**, *135*, 10294-10297.

(17) Stock, N.; Biswas, S. Synthesis of Metal-Organic Frameworks (MOFs): Routes to Various MOF Topologies, Morphologies, and Composites. *Chem. Rev.* **2012**, *112*, 933-969.

(18) Férey, G.; Serre, C.; Mellot-Draznieks, C.; Millange, F.; Surblé, S.; Dutour, J.; Margiolaki, I. A Hybrid Solid with Giant Pores Prepared by a Combination of Targeted Chemistry, Simulation, and Powder Diffraction. *Angew. Chem. Int. Ed.* **2004**, *43*, 6296-6301.

(19) Cavka, J. H.; Jakobsen, S.; Olsbye, U.; Guillou, N.; Lamberti, C.; Bordiga, S.; Lillerud, K. P. A New Zirconium Inorganic Building Brick Forming Metal–Organic Frameworks with Exceptional Stability. *J. Am. Chem. Soc.* **2008**, *130*, 13850-13851.

(20) Chui, S. S.-Y.; Lo, S. M.-F.; Charmant, J. P. H.; Orpen, A. G.; Williams, I. D. A Chemically Functionalizable Nanoporous Material $[Cu_3(TMA)_2(H_2O)_3]_n$. *Science* **1999**, *283*, 1148-1150.

(21) Ahrenholtz, S. R.; Epley, C. C.; Morris, A. J. Solvothermal Preparation of an Electrocatalytic Metalloporphyrin MOF Thin Film and its Redox Hopping Charge-Transfer Mechanism. *J. Am. Chem. Soc.* **2014**, *136*, 2464-2472.

(22) Dou, J.-H.; Sun, L.; Ge, Y.; Li, W.; Hendon, C. H.; Li, J.; Gul, S.; Yano, J.; Stach, E. A.; Dincă, M. Signature of Metallic Behavior in the Metal–Organic Frameworks M_3(hexaiminobenzene)$_2$ (M = Ni, Cu). *J. Am. Chem. Soc.* **2017**, *139*, 13608-13611.

(23) Wu, G.; Huang, J.; Zang, Y.; He, J.; Xu, G. Porous Field-Effect Transistors Based on a Semiconductive Metal–Organic Framework. *J. Am. Chem. Soc.* **2017**, *139*, 1360-1363.

(24) Clough, A. J.; Skelton, J. M.; Downes, C. A.; de la Rosa, A. A.; Yoo, J. W.; Walsh, A.; Melot, B. C.; Marinescu, S. C. Metallic Conductivity in a Two-Dimensional Cobalt Dithiolene Metal–Organic Framework. *J. Am. Chem. Soc.* **2017**, *139*, 10863-10867.

(25) Clough, A. J.; Yoo, J. W.; Mecklenburg, M. H.; Marinescu, S. C. Two-Dimensional Metal–Organic Surfaces for Efficient Hydrogen Evolution from Water. *J. Am. Chem. Soc.* **2015**, *137*, 118-121.

(26) Kobayashi, Y.; Jacobs, B.; Allendorf, M. D.; Long, J. R. Conductivity, Doping, and Redox Chemistry of a Microporous Dithiolene-Based Metal–Organic Framework. *Chem. Mater.* **2010**, *22*, 4120-4122.

(27) Foster, M. E.; Sohlberg, K.; Allendorf, M. D.; Talin, A. A. Unraveling the Semiconducting/Metallic Discrepancy in $Ni_3(HITP)_2$. *J. Phys. Chem. Lett.* **2018**, *9*, 481-486.

(28) Ko, M.; Mendecki, L.; Mirica, K. A. Conductive Two-Dimensional Metal–Organic Frameworks as Multifunctional Materials. *Chem. Commun.* **2018**, *54*, 7873-7891.

(29) Yang, C.; Dong, R.; Wang, M.; Petkov, P. S.; Zhang, Z.; Wang, M.; Han, P.; Ballabio, M.; Bräuninger, S. A.; Liao, Z.; Zhang, J.; Schwotzer, F.; Zschech, E.; Klauss, H.-H.; Cánovas, E.; Kaskel, S.; Bonn, M.; Zhou, S.; Heine, T.; Feng, X. A Semiconducting Layered Metal-Organic Framework Magnet. *Nature Commun.* **2019**, *10*, 3260.

(30) Usman, M.; Mendiratta, S.; Lu, K.-L. Semiconductor Metal–Organic Frameworks: Future Low-Bandgap Materials. *Advanced* **2017**, *10*, 1605071.

(31) Xie, L. S.; Skorupskii, G.; Dincă, M. Electrically Conductive Metal–Organic Frameworks. *Chem. Rev.* **2020**, *120*, 8536-8580.

(32) Givaja, G.; Amo-Ochoa, P.; Gómez-García, C. J.; Zamora, F. Electrical Conductive Coordination Polymers. *Chem. Soc. Rev.* **2012**, *41*, 115-147.

(33) Xie, J.; Ewing, S.; Boyn, J.-N.; Filatov, A. S.; Cheng, B.; Ma, T.; Grocke, G. L.; Zhao, N.; Itani, R.; Sun, X.; Cho, H.; Chen, Z.; Chapman, K. W.; Patel, S. N.; Talapin, D. V.; Park, J.; Mazziotti, D. A.; Anderson, J. S. Intrinsic Glassy-Metallic Transport in an Amorphous Coordination Polymer. *Nature* **2022**, *611*, 479-484.

(34) Vicent-Morales, M.; Esteve-Rochina, M.; Calbo, J.; Ortí, E.; Vitórica-Yrezábal, I. J.; Mínguez Espallargas, G. Semiconductor Porous Hydrogen-Bonded Organic Frameworks Based on Tetrathiafulvalene Derivatives. *J. Am. Chem. Soc.* **2022**, *144*, 9074-9082.

(35) Frischmann, P. D.; Mahata, K.; Würthner, F. Powering the Future of Molecular Artificial Photosynthesis with Light-Harvesting Metallosupramolecular Dye Assemblies. *Chem. Soc. Rev.* **2013**, *42*, 1847-1870.

(36) Logsdon, J. L.; Hartnett, P. E.; Nelson, J. N.; Harris, M. A.; Marks, T. J.; Wasielewski, M. R. Charge Separation Mechanisms in Ordered Films of Self-Assembled Donor–Acceptor Dyad Ribbons. *ACS Appl. Mater. Interfaces* **2017**, *9*, 33493-33503.

(37) Lin, S.; Diercks, C. S.; Zhang, Y.-B.; Kornienko, N.; Nichols, E. M.; Zhao, Y.; Paris, A. R.; Kim, D.; Yang, P.; Yaghi, O. M.; Chang, C. J. Covalent Organic Frameworks Comprising Cobalt Porphyrins for Catalytic CO_2 Reduction in Water. *Science* **2015**, *349*, 1208-1213.

(38) Xing, Y.; Park, T.-H.; Venkatramani, R.; Keinan, S.; Beratan, D. N.; Therien, M. J.; Borguet, E. Optimizing Single-Molecule Conductivity of Conjugated Organic Oligomers with Carbodithioate Linkers. *J. Am. Chem. Soc.* **2010**, *132*, 7946-7956.

(39) Grosso, G.; Parravicini, G. P. Solid State Physics. 2nd ed.; Grosso, G., Parravicini, G. P. Eds.; 2014; pp 483-528.

(40) Sun, L.; Campbell, M. G.; Dincă, M. Electrically Conductive Porous Metal–Organic Frameworks. *Angew. Chem. Int. Ed.* **2016**, *55*, 3566-3579.

(41) Conductivity of 10^{-8}-to-10^{-4} S/cm should satisfy the requirements in the molecular PEC energy conversion scheme; i.e., when applied to micron-scale structures that harvest light at an intensity of 1 sun, such conductivities are large enough to preclude significant iR loss-es

(42) Nelson, A. P.; Farha, O. K.; Mulfort, K. L.; Hupp, J. T. Supercritical Processing as a Route to High Internal Surface Areas and Permanent Microporosity in Metal–Organic Framework Materials. *J. Am. Chem. Soc.* **2009**, *131*, 458-460.

(43) Snellenburg, J. J.; Laptenok, S.; Seger, R.; Mullen, K. M.; van Stokkum, I. H. M. Glotaran: A Java-Based Graphical User Interface for the R Package TIMP. *J. Stat. Softw.* **2012**, *49*.

(44) The damage can be irreversible if evacuated from polar solvent and/or harsh condition (fast vacuum under heat).

(45) Deria, P.; Gómez-Gualdrón, D. A.; Bury, W.; Schaef, H. T.; Wang, T. C.; Thallapally, P. K.; Sarjeant, A. A.; Snurr, R. Q.; Hupp, J. T.; Farha, O. K. Ultraporous, Water Stable, and Breathing Zirconium-Based Metal–Organic Frameworks with ftw Topology. *J. Am. Chem. Soc.* **2015**, *137*, 13183-13190.

(46) Yu, J.; Anderson, R.; Li, X.; Xu, W.; Goswami, S.; Surendran Rajasree, S.; Maindan, K.; Gómez-Gualdrón, D. A.; Deria, P. Improving Energy Transfer within Metal-Organic Frameworks by Aligning Linker Transition Dipole along Framework Axis. *J. Am. Chem. Soc.* **2020**, *142*, 11192-11202.

(47) Furlani, C.; Luciani, L. Complexes of Dithiocarboxylic Acids. *Inorg. Chem.* **1968**, *7*, 1586-1592.

(48) Data collected for Spiro-CS_2Ni suggest a low density sample that limited the extent of spectral resolution and possibility of a subsequent 2D ^1H – ^{13}C HETCOR experiment (to determine structural information through the ^1H spin diffusion to ^{13}C). Nevertheless, the broad spectra did not indicate presence of any 'isolated' hetergeniety within the polymer.

(49) Bennett, T. D.; Cheetham, A. K. Amorphous Metal–Organic Frameworks. *Acc. Chem. Res.* **2014**, *47*, 1555-1562.

(50) McGreevy, R. L. Reverse Monte Carlo Modelling. *J. Phys.: Condens. Matter* **2001**, *13*, R877.

(51) Anderson, R.; Gómez-Gualdrón, D. A. Increasing Topological Diversity During Computational "Synthesis" of Porous Crystals: How and Why. *CrystEngComm* **2019**, *21*, 1653-1665.

(52) Irreversible redox peaks for these MOF deposited working electrodes seem to stem from different charge-transfer kinetics for the forward and reverse process involving mass transfer of the counterions, this is validated by using a different elec-trode surface where the reverse current appears but at a potential with large ΔE(peak) -indicating kinetic involvement of trapped counterions.

(53) Spiro-CS_2Ni displayed a $\sigma = 1.4 \times 10^{-6}$ S/cm at +1.5 V (see Figure S6)

(54) Redox conductivity values established for relevant benchmark polymeric solids are: Mn_2-DSBDC, $\sigma = 10^{-6}$ S/cm (see ref. 40); iodine-doped Cu[Cu(pdt)$_2$] and Cu[Ni(pdt)$_2$], $\sigma = 10^{-4}$ S/cm (see ref 26); graphene-like cobalt-dithiolene 2D-MOFs, $\sigma = 10^{-3}$ S/cm (ref 24); and MOF with poly-thiophene in its meso-pores, $\sigma = 1.3\times10^{-7}$ S/cm (see: ACS Appl. Mater. Interfaces 2017, 14, 12584).

(55) The electrochemical measurements mentioned above (i.e., CV, impedance spectra) were performed on dried films after EPD.

(56) Aragonès, A. C.; Martín-Rodríguez, A.; Aravena, D.; Puigmartí-Luis, J.; Amabilino, D. B.; Aliaga-Alcalde, N.; González-Campo, A.; Ruiz, E.; Díez-Pérez, I. Tuning Single-Molecule Conductance in Metalloporphyrin-Based Wires via Supramolecular Interactions. *Angew. Chem. Int. Ed.* **2020**, *59*, 19193-19201.

(57) Ogawa, S.; Chattopadhyay, S.; Tanaka, Y.; Ohto, T.; Tada, T.; Tada, H.; Fujii, S.; Nishino, T.; Akita, M. Control of Dominant Conduction Orbitals by Peripheral Substituents in Paddle-wheel Diruthenium Alkynyl Molecular Junctions. *Chem. Sci.* **2021**, *12*, 10871-10877.

(58) Huang, P.-J.; Natori, Y.; Kitagawa, Y.; Sekine, Y.; Kosaka, W.; Miyasaka, H. One-Dimensional Chains of Paddlewheel-Type Dichromium(II,II) Tetraacetate Complexes: Study of Electronic Structure Influenced by σ- and π-Donation of Axial Linkers. *Inorg. Chem.* **2018**, *57*, 5371-5379.

(59) Aragonès, A. C.; Darwish, N.; Saletra, W. J.; Pérez-García, L.; Sanz, F.; Puigmartí-Luis, J.; Amabilino, D. B.; Díez-Pérez, I. Highly Conductive Single-Molecule Wires with Controlled Orientation by Coordination of Metalloporphyrins. *Nano Lett.* **2014**, *14*, 4751-4756.

(60) Maindan, K.; Li, X.; Yu, J.; Deria, P. Controlling Charge-Transport in Metal–Organic Frameworks: Contribution of Topological and Spin-State Variation on the Fe-Porphyrin Centered Redox Hopping Rate. *J. Phys. Chem. B* **2019**, *123*, 8814-8822.

(61) Liberman, I.; Shimoni, R.; Ifraemov, R.; Rozenberg, I.; Singh, C.; Hod, I. Active-Site Modulation in an Fe-Porphyrin-Based Metal–Organic Framework through Ligand Axial Coordination: Accelerating Electrocatalysis and Charge-Transport Kinetics. *J. Am. Chem. Soc.* **2020**, *142*, 1933-1940.

(62) Two MIM coordination would lead the complex to adopt a distorted octahedral coordination with two elongated Ni-S bonds, which plays a role to Ni-CS_2R disintegration

(63) This is to ensure an average and comparable degree of unwanted network stacking or proximity contributing to electronic properties

(64) Martin, R. L. Natural Transition Orbitals. *J. Chem. Phys.* **2003**, *118*, 4775-4777.

(65) Due to scattering, only the red side can be seen in Figure 6b

(66) Note that the current data with scattering sample did not lead to a complete deconvoluted SAS of B; a clear SAS signature of the B was obtained from the ns-TA data recorded with 532 nm excitation (Figure S25)

(67) Given the mixed nature of frontier orbitals it is not clear the chemical structural components that host of the respective charge carriers; it can only be presumed from the 0.55 V electrochemical potential gap between the first '(—CS_2)$_2$Ni' –centric and second spirofluorene centered reduction peeks that upon photoexcitation, PCT from spirofluorene to '(—CS_2)$_2$Ni' may be in place.

(68) No sizable HER was observed for Spiro-CS_2Ni@FTO until -1 V

(69) Peter, L. M. Dynamic Aspects of Semiconductor Photoelectrochemistry. *Chem. Rev.* **1990**, *90*, 753-769.

(70) Note that although a fair ligand exchange was observed for MIM in organic solvent, the Spiro-CS_2Ni appears to be robust in strong aqueous acid and base (pH = 2-12), albeit a hint of leaching was observed after it was left submerged for a week; nevertheless, the residual solid maintains integrity (see Figure S27-29)

TOC: